



Large-scale Magnetic Funnels in the Solar Corona

Olga Panasenco¹, Marco Velli², and Aram Panasenco^{1,3}
¹ Advanced Heliophysics, Pasadena, CA 91106, USA; panasenco.olga@gmail.com

² EPSS, UCLA, Los Angeles, CA 90095, USA

³ Department of Mathematics, UCLA, Los Angeles, CA 90095, USA

Received 2018 March 13; revised 2019 January 19; accepted 2019 January 22; published 2019 February 28

Abstract

We describe open coronal magnetic fields with a specific geometry—*large-scale coronal magnetic funnels*—that are found to play an important role in coronal dynamics. Coronal magnetic funnels can be attributed to three main factors: (i) the presence of pseudostreamer(s), (ii) the presence of filament channels, and (iii) the presence of active regions in the close vicinity of a pseudostreamer. The geometry of magnetic funnels displays a strongly nonmonotonic expansion below $2 R_{\odot}$. We present a detailed study of a funnel arising from a double pseudostreamer near the equator, formed between a triplet of coronal holes of the same polarity. By following the evolution of these coronal holes we find that the pseudostreamer and, therefore, funnel topology, changes when two coronal holes have merged together. The funnel geometry of the open magnetic field becomes smoother, with a monotonic expansion factor, after this merging. The presence of magnetic funnels is indirectly confirmed by the appearance of coronal cloud prominences in the solar corona, typically in the 304 Å passband, as a result of colder plasma debris falling back toward the Sun in the wake of eruptions in the surrounding atmosphere. The coronal clouds appear suspended at heights of 1.2–1.3 R_{\odot} , coinciding with the region of strongest gradients in the magnetic field. By studying the evolution of funnel open magnetic fields over several solar rotations we find a direct relation between the presence of coronal clouds high in the solar corona and the coincident existence of funnel magnetic fields below them.

Key words: solar wind – Sun: activity – Sun: corona – Sun: coronal mass ejections (CMEs) – Sun: filaments, prominences – Sun: magnetic fields

Supporting material: animation

1. Introduction

In this paper we describe and trace the evolution of large-scale magnetic *funnels* in the solar corona. Funnels are one of many ways in which the interplay of the solar magnetic field and solar coronal expansion structures the solar corona, and they are interesting because they explain the consistent appearance of a specific type of prominence, the so-called coronal cloud prominences, in the same coronal location over long periods of time. Coronal cloud prominences, or coronal clouds for short, are parcels of plasma, usually observed in the 304 Å and H α channels, appearing to levitate high in the corona and being observed during, as well as in the hours immediately following, solar eruptions both nearby and far away (see Figure 1). We describe coronal clouds observed with the *Solar Dynamics Observatory* (*SDO*) and *STEREO* during the month of 2012 September at the same location in the solar corona but over widely separated periods in time (Table 1) and investigate why these peculiar types of prominences appear at different times in the same coronal structure. We find a strong correlation between coronal cloud formation and filament activation, eruptions, and coronal mass ejections (CMEs) occurring nearby.

Solar eruptions come in many shapes and sizes, and though their outcome consists mostly of plasma lost in interplanetary space, the loss is never complete, and is often if not always accompanied by plasma falling back down into the solar atmosphere. In some cases the connection between eruptions and inflows is obvious and apparent, such as in spectacular failed or partially failed eruptions. Other times it is less so: for example, coronal inflows, identified as small features moving

inward in the inner and outer white-light corona at heliospheric distances below $5 R_{\odot}$ (Wang et al. 1999; Sheeley & Wang 2002, 2014; Hess & Wang 2017) were seen in the *Solar and Heliospheric Observatory* (*SOHO*)/Large Angle and Spectromeric Coronagraph Experiment (LASCO) C2 coronagraph field of view not to have clearly identifiable counterparts moving outward. However, as shown in Hess & Wang (2017), most of these inner-coronal inflows are indeed closely associated with CMEs, being observed during and in the days immediately following the eruptions.

Hess & Wang (2017), using white-light observations from LASCO C2 and *STEREO*/COR1, described inflows associated with CMEs as the closing-down of very high loops and open flux in the wake of CMEs originated from helmet streamers. CMEs that originated from pseudostreamers have different morphologies. Pseudostreamers separate coronal holes of the same polarity and often harbor one or two solar filaments in their base; filament channel arcades become part of the pseudostreamer lobes (Wang et al. 2007; Panasenco & Velli 2010, 2013). CMEs from pseudostreamers have different structures compare to CMEs from helmet streamers. As described in Wang (2015) and Wang & Hess (2018a, 2018b) pseudostreamer CMEs tend to have a narrow fan-like morphology and to be smaller and weaker than the CMEs associated with helmet streamers.

Wang & Hess (2018b) show that the visibility of the inflows depends on the amount of material that the diverging components sweep up within the $2\text{--}6 R_{\odot}$ field of view and that the rate of inflow production tends to increase when a helmet streamer is activated by underlying flux emergence. Wang & Hess (2018a) show that, for CMEs that originated

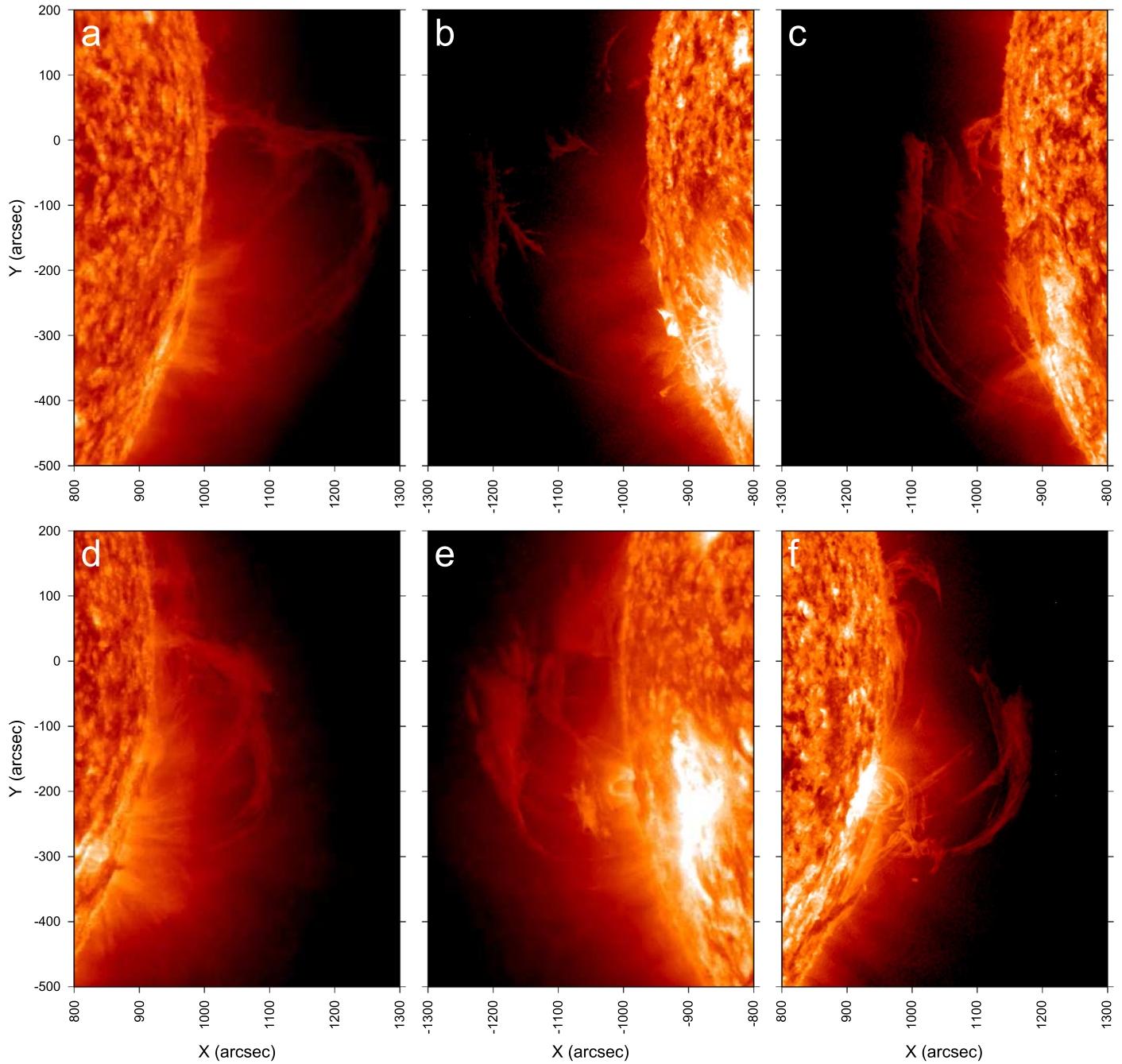


Figure 1. Coronal cloud prominences observed in the 304 Å channel from multiple spacecraft at different times but located in the same magnetic funnel: (a) view of the west limb from *STEREO/SECCHI-A* on 2012 August 28, 11:46 UT; (b) on the east limb from *SDO/AIA* on 2012 September 1, 13:39 UT; (c) on the east limb from *SDO/AIA* on 2012 September 3, 00:39 UT; (d) on the west limb from *STEREO/SECCHI-B* on 2012 September 5, 12:26 UT; (e) on the east limb from *STEREO/SECCHI-A* on 2012 September 10, 7:36 UT; and (f) on the west limb from *SDO/AIA* on 2012 September 13, 19:29 UT. The animation of the sequence shown in panels (b) and (c) starts at 2012 August 31 00:00:31Z and ends at 2012 September 3 23:59:19Z. The video duration is 115 s.

(An animation of this figure is available.)

from pseudostreamers, only a small number of inflows were detected. However, the very faint low-density features in pseudostreamer events suggests that more inflows may be present at or below the noise level of the COR1 instrument (Wang & Hess 2018a, 2018b). In this paper we propose that inflows in the wake of pseudostreamer CMEs exist nearly always, but due to the weaker and more disperse nature of these CMEs and the deflection of the CMEs in the low corona below $3\text{--}4 R_{\odot}$ shown in Panasenco et al. (2013) and

Liewer et al. (2013, 2015), the size of such low-density inflows will be very small and more widely dispersed as they originate from much smaller heights compared to helmet CME inflows.

Historically, the formation of “suspended clouds” and “coronal spiders” was linked to thermal instabilities and coronal condensations (Engvold 1976; Allen et al. 1998; Lin et al. 2006; Stenborg et al. 2008; Liu et al. 2012). But this process is unlikely to play a primary role because of the limited amount of mass—enough to account at most for two well-developed

Table 1
Coronal Cloud Observations

Time Period	Observatory	Limb
Aug 28–29	STEREO-A	west
Aug 30–Sep 3	SDO	east
Sep 5–8	STEREO-B	west
Sep 10–11	STEREO-A	east
Sep 14–16	SDO	west
Sep 19	STEREO-B	east
Sep 24–25	STEREO-A	west

filaments (Saito & Tandberg-Hanssen 1973; Mackay 2005)—globally available in the corona at any given time.

The coronal cloud prominences discussed in this paper are observed high in the corona as illustrated in Figure 1 and should be distinguished from other cloud-like structures that form inside filament channel systems at much lower heights after confined filament eruptions, as described in Liu et al. (2012). For these latter types, the filament plasma does not escape the arcade arching above the channel and, therefore, does not propagate out high into the corona, but moves mostly inside and along the filament channel itself. The small-scale inflows after pseudostreamer and helmet streamer CMEs, described in Hess & Wang (2017) and Wang & Hess (2018a, 2018b), appear to be the main sources of plasma for coronal cloud prominences—small plasma leftovers of nearby erupted filaments—cores of CMEs. In our study of 19 CMEs (Table 2), the major filament eruption of 2012 August 31, depicted in Figure 2, serves as the prime example for the sequence of events linking the eruption of a filament to the formation of coronal clouds, preceding and following by total 18 more eruptions over the period described in this study from 2012 August 28–September 25. Figure 3 illustrates the magnetic configuration in the environment where coronal clouds are seen to form. The right-hand panels provide magnetic field pressure contours at a height of $1.085 R_{\odot}$ with the areas of coronal holes shown shaded in blue and the position of filament channels indicated by the dotted red lines. Left-hand panels show magnetic field lines overlaid on HMI magnetograms for the funnel forming region. Top and bottom panels show the same region one solar rotation apart. The top panels provide reconstructions at the time of coronal cloud formation, when the open field line regions were confined to two narrow strips harboring two filament channel arcades of closed loops, while by the time of the magnetic field maps of the bottom panels, from observations a month later, the coronal cloud had disappeared, and the two narrow coronal holes had merged together into a recognizable wide coronal hole erasing Area 2 with two filaments.

On 2012 August 31, the erupting material was deflected by the neighboring coronal holes into the funnel region, as indicated by the arrows in Figure 3, and in the animation associated with panels (b) and (c) in Figure 1. The widely dispersed ($\sim 80^{\circ}$ – 100° in longitude) material falling back from prior eruption(s) into funnel-like coronal magnetic configurations leads to the observed formation of coronal clouds high in the solar corona. The strong divergence of funnel open field lines below $2 R_{\odot}$ works like a wide net that captures the falling back post-eruptive material. The levitation and subsequent draining of the cloud is reasonably explained by the balance of

Table 2
Eruptions (2012 August–September)

#	Data (2012)	Time (UT)	Area	Observatory
1	Aug 28	14:36	1	STEREO-B
2	Aug 29	10:26	1	STEREO-B
3	Aug 31	11:20	2	STEREO-B
4	Aug 31	19:45	4	SDO
5	Sep 2	01:06	1	STEREO-B
6	Sep 3	11:00	1	STEREO-B
7	Sep 4	11:30	2	SDO
8	Sep 4	23:26	1	STEREO-B
9	Sep 5	09:45	2	SDO
10	Sep 8	05:00	1	SDO
11	Sep 9	19:00	2	SDO
12	Sep 9	21:30	1	SDO
13	Sep 10	04:55	3	SDO
14	Sep 13	07:50	1	SDO
15	Sep 16	00:06	2	STEREO-A
16	Sep 20	20:45	2	STEREO-A
17	Sep 21	05:20	2	STEREO-A
18	Sep 21	17:05	2	STEREO-A
19	Sep 24	22:30	2	STEREO-B

forces provided by the funnel magnetic field configuration, together with the diamagnetic properties of the plasma clouds.

As a result coronal clouds act as tracers of peculiar magnetic field configurations where narrow lanes of magnetic field expand dramatically into the upper corona and into the solar wind. Such configurations may be a source of specific solar wind types and may therefore also be relevant in understanding solar wind origins. We defer such a study to future work. Here we focus on a systematic investigation of coronal clouds observed by SDO and both STEREO spacecraft, reconstructing the magnetic field configurations at the time of the clouds by using a PFSS model to extrapolate the magnetic environments supporting levitating coronal clouds.

To understand what happens to the returning mass, we reconstruct spatial slices showing the global coronal magnetic configurations adjacent to the eruptive sites. In this way we can determine the possible locations where erupting filament plasma, when falling back to the surface, may be temporarily decelerated and confined to form the coronal clouds. The next section reports the most significant multispacecraft coronal cloud prominence observations we have used to understand the formation of the funnel-like magnetic configuration of the corona. In Section 3 we discuss the magnetic field structure of the coronal funnels where clouds appear and in Section 4 we compare the forces acting on coronal cloud prominences, which we interpret as diamagnetic plasma blobs or plasmoids. Finally, Section 5 provides a summary and conclusions.

2. Coronal Multispacecraft Observations

The consecutive CMEs and limb coronal clouds studied in this paper were observed by multiple spacecraft from 2012 August 28–September 25 (Table 1). Figure 1 shows a sequence of coronal cloud prominences observed by STEREO and SDO on the east and west limbs of the Sun over a period of 18 days in 2012 August and September. Each image of the sequence gives a snapshot of a coronal cloud prominence that formed over a period of about an hour. The plasma is then seen to slowly drain down toward the chromosphere over a period of several hours (we define the cloud formation time as the

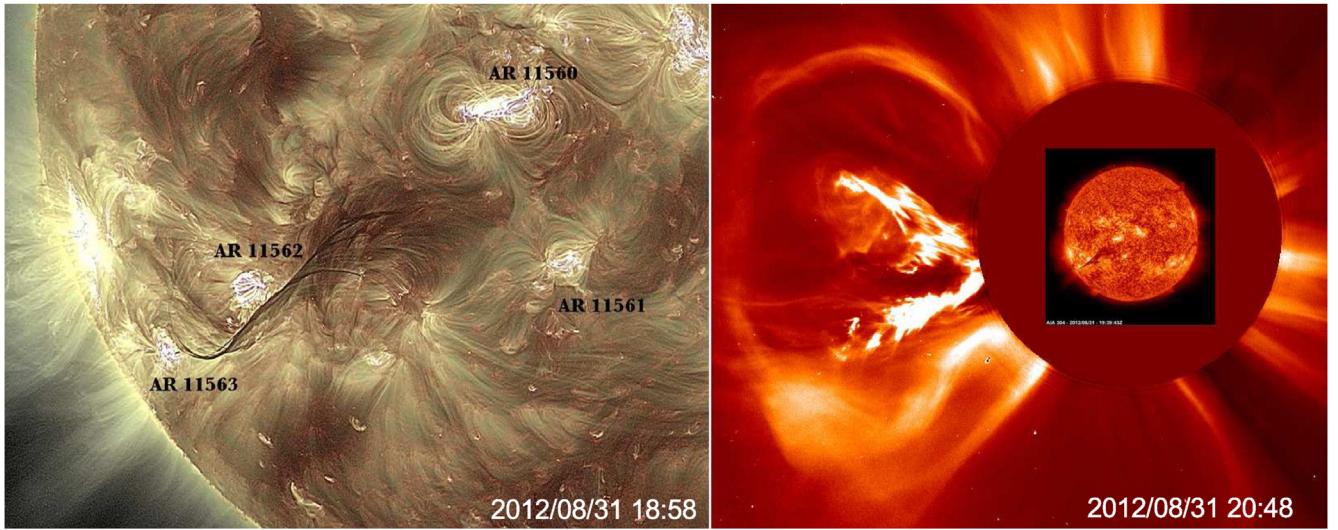


Figure 2. Filament prior to the eruption and subsequent nonradial CME on 2012 August 31 as observed by *SDO/AIA* (superposition of the 193 and 171 Å AIA channels, left panel) and superposition of *SOHO/LASCO* C2 and *SDO/AIA* 304 Å (right panel). This filament was located in Area 4 in Figure 3 and has number 4 in Table 2. The cloud started to form within hours after this eruption at the east limb at the same latitude as the filament location, at a separation of about 100° in longitude.

interval from the moment when the first parcels of plasma appear in the corona to the moment when the down-draining motion begins; after the formation period the plasma accumulation and drainage continue simultaneously). The cloud prominence in each snapshot formed in the same region of the solar atmosphere, the material beginning to collect at a similar height of about $\sim 0.2 R_{\odot}$ above the surface (R_{\odot} is the solar radius) and then slowly spreading to the sides and draining down. The origin of the mass in the clouds appears to be debris from one or more eruptions occurring in regions neighboring the one where the cloud prominence formed, though in some instances the location of the eruption supplying plasma to coronal cloud prominences was as far as $\sim 80^{\circ}$ in longitude (Figures 2 and 3, Table 2). When the source of the clouds was so far, the originating eruptions were not radial, rather the erupting filament suffered strong deflections from neighboring structures, such as coronal holes (Panasenco et al. 2011, 2013), sufficient to bring plasma to the region where it could then fall back to the Sun and accumulate into the observed coronal clouds.

Figure 1(a) shows the coronal cloud prominence observed on 2012 August 28. It started to form at 8:00 UT, after a previous eruption of an active region filament observed by *STEREO-B*, and reached its maximum development at 10:30 UT. By 16:00 UT the cloud had drained away.

Figures 1(b), (c) show coronal cloud prominences that formed after the eruption of a huge filament from the southeast quadrant on 2012 August 31 shown in Figure 2. This major filament eruption produced a CME with speed $\sim 1100 \text{ km s}^{-1}$ and a nonradial deflection of $\sim 40^{\circ}$ toward the coronal cloud formation area. The northeast direction of the deflection was caused by the coronal holes located on the southern and northwestern sides of the erupting filament in Area 4. Such deflections were described in detail by Panasenco et al. (2011, 2013) and Liewer et al. (2013, 2015). Three hours after the eruption an especially dense coronal cloud started to form at a height of $\sim 0.2 R_{\odot}$ above the surface growing in volume very fast and draining down very soon after the first appearance (~ 40 minutes), with typical downfall speeds of $\sim 60\text{--}80 \text{ km s}^{-1}$

as we will show using time-slice diagrams later. The main bulk of plasma falling back after the eruption arrived later and the coronal cloud prominence reached its maximum extent at the end of 2012 September 1. Plasma was constantly supplied to the cloud and drained down over approximately 2 days (Figures 1(b), (c)). The plasma then drained down toward the photosphere along a number of discrete well-defined paths. The number of draining trajectories was small and, for the case of September 1–3, only about 4–5 different trajectories could be counted in the limb projection (Figure 5, left).

The downflow trajectories are very few but stable, closely following the closed loops adjacent to the open field of the funnel in the PFSS reconstruction. These loops belong to the filament channel overlying the arcade adjacent to the funnel (white lines in Figure 3, top left). The downflow of plasma was traced directly into the filament channel on September 1, 13:59 UT by limb observations from *SDO/AIA* and disk observations from *STEREO-B* in 304 Å channel.

Table 2 lists 19 eruptions that occurred in the vicinity of our coronal cloud formation region, most of these being sympathetic eruptions originating from the four lobes of the double pseudostreamer described here. Sympathetic eruptions from pseudostreamer lobes are a relatively common phenomenon (Panasenco & Velli 2010; Török et al. 2011; Wang & Hess 2018a). In the case of major eruptions plasma debris accumulates gradually during a relatively long period of time (1–2 hr) creating a long lived source of plasma up in the corona. The coronal cloud observed in 304 Å usually forms on the same timescale and then drains down over longer timescales of 24–48 hr. The magnetic structure that supports the coronal clouds very rarely drains completely as it is continuously resupplied. Most of the plasma debris falling through the corona may be captured by the open magnetic funnel fields, nestling into the funnel’s narrowest regions and accumulating there until the densities become sufficient to be observable in the 304 Å helium band. Indeed, the coronal cloud is best visible in the 304 Å band, however, the very bottom of the 304 Å cloud may also be visible in 171 Å as a thin narrow line. This is visible in the left panel of

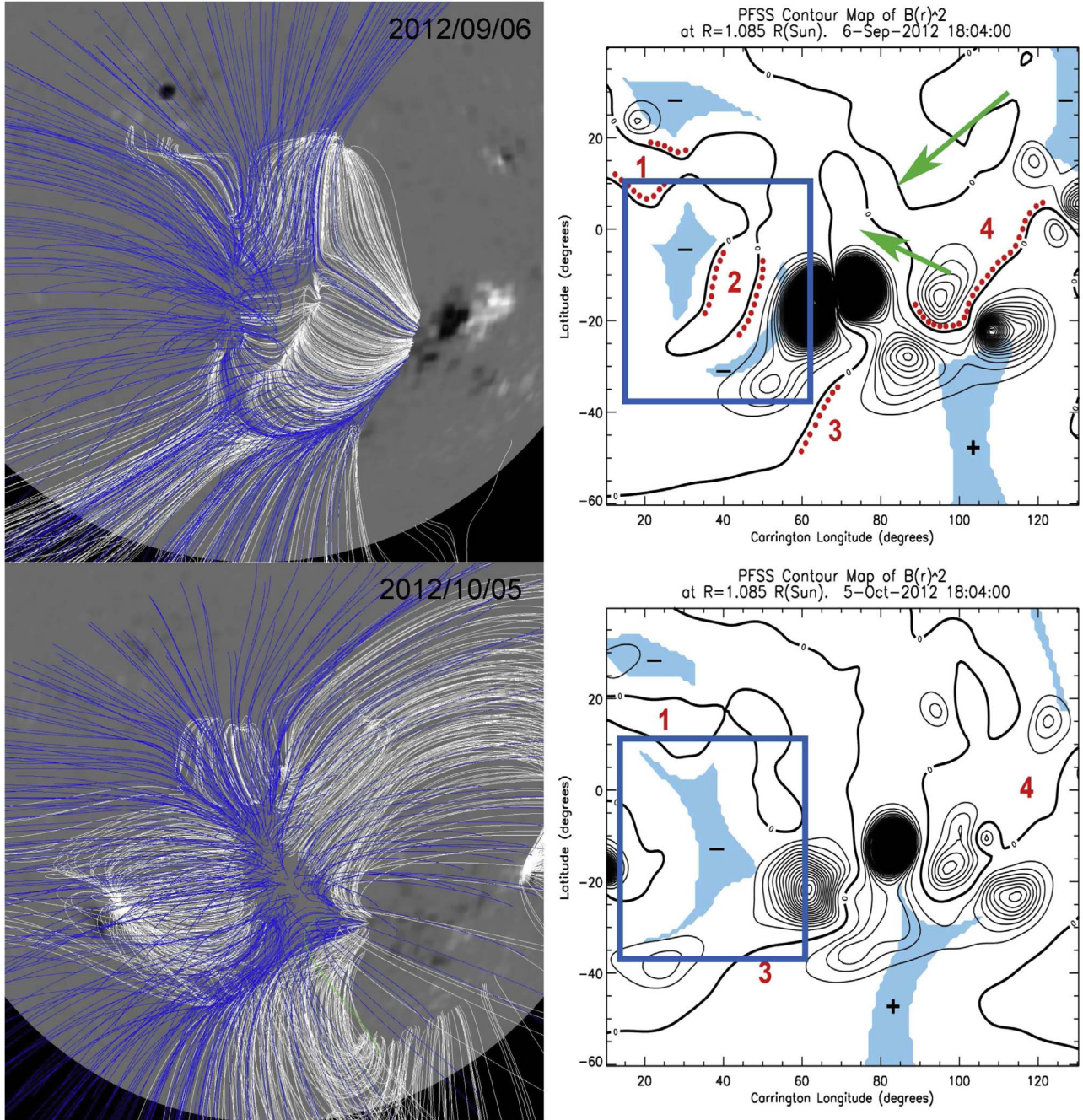


Figure 3. Top left: solar magnetogram with overlying magnetic field lines obtained via a PFSS model in the regions neighboring the coronal funnel. White field lines close below the source surface, blue lines are open. Coronal clouds form in the narrow open field region bounded by closed lines. Top right panel: magnetic pressure contours at the height of $1.085 R_{\odot}$ with the area covered by open field lines shaded in blue. The rectangle shows that the left panel corresponds to a smaller region than the one shown on the right. Red dots illustrate position of filament channels on the solar disk. The green arrows indicate the direction of deflections of the erupting material originating in Area 4. Bottom left panel: same region as top left seen one rotation later, when the magnetic funnel has disappeared. Bottom right: same as top right seen one rotation later. Numbers correspond to the areas listed in Table 2.

Figure 4 as the thin dark region above the limb roughly parallel to the solar surface and indicated by the arrow. The right-hand panel shows the same region a few hours later once the cloud has disappeared from the 171 \AA band. To the south of the funnel one may see a negative image of what is actually a pseudostreamer configuration, identified by the second arrow and also visible in the PFSS reconstruction, shown in Figure 10. The presence of the hotter plasma at the bottom of the coronal cloud can be explained by plasma compression during accumulation in the narrowest part of the

magnetic funnel. Interestingly, the 171 \AA draining trajectories coincide with 304 \AA ones.

Coronal clouds form by gradually accumulating material high in the corona that subsequently drains slowly down toward the chromosphere along a few well-defined paths. Figure 5 shows the coronal cloud prominences observed on the limb in the 304 \AA band by SDO on 2012 September 1 and 13. We used eight cuts to create time-slice diagrams for the cloud region following the plasma draining trajectories, shown in Figures 6 and 7.

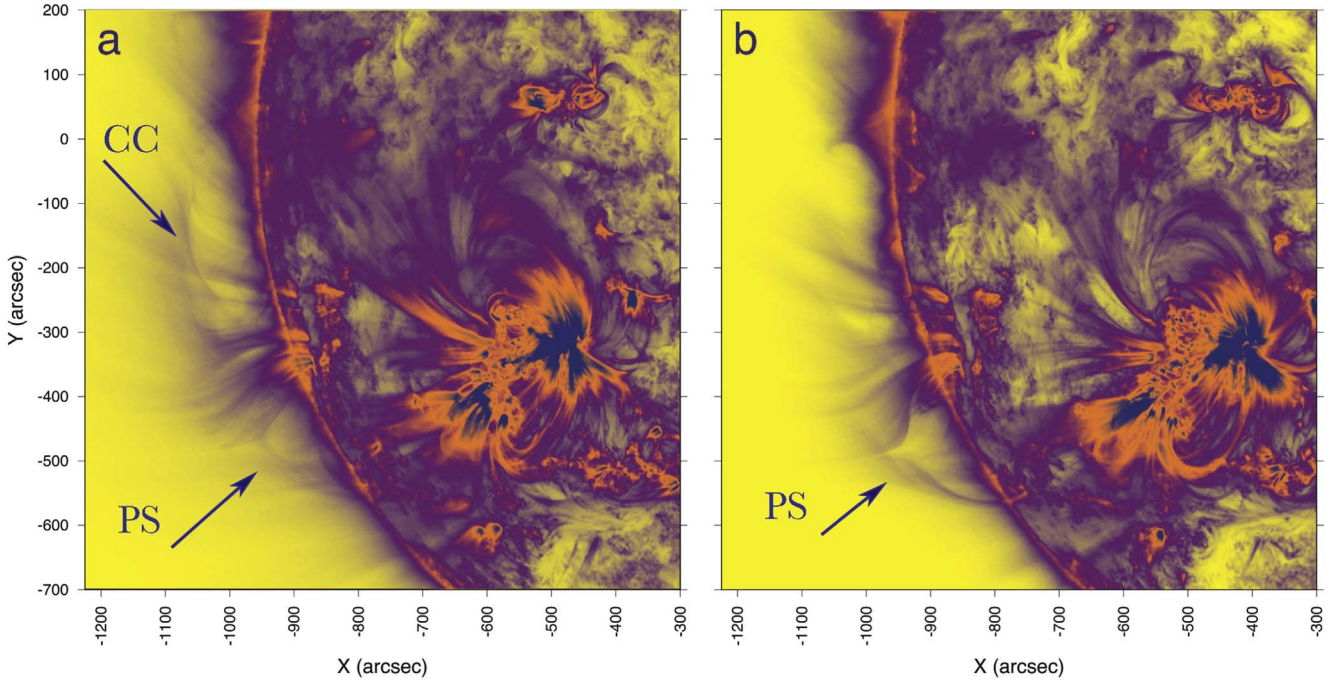


Figure 4. Coronal cloud CC (left panel) and the corona observed by *SDO/AIA* in the 171 Å channel on 2012 September 3 at 10:31 UT (left panel) and 17:55 UT (right panel). The pseudostreamer lobes (PS) are visible to the south of the coronal cloud location.

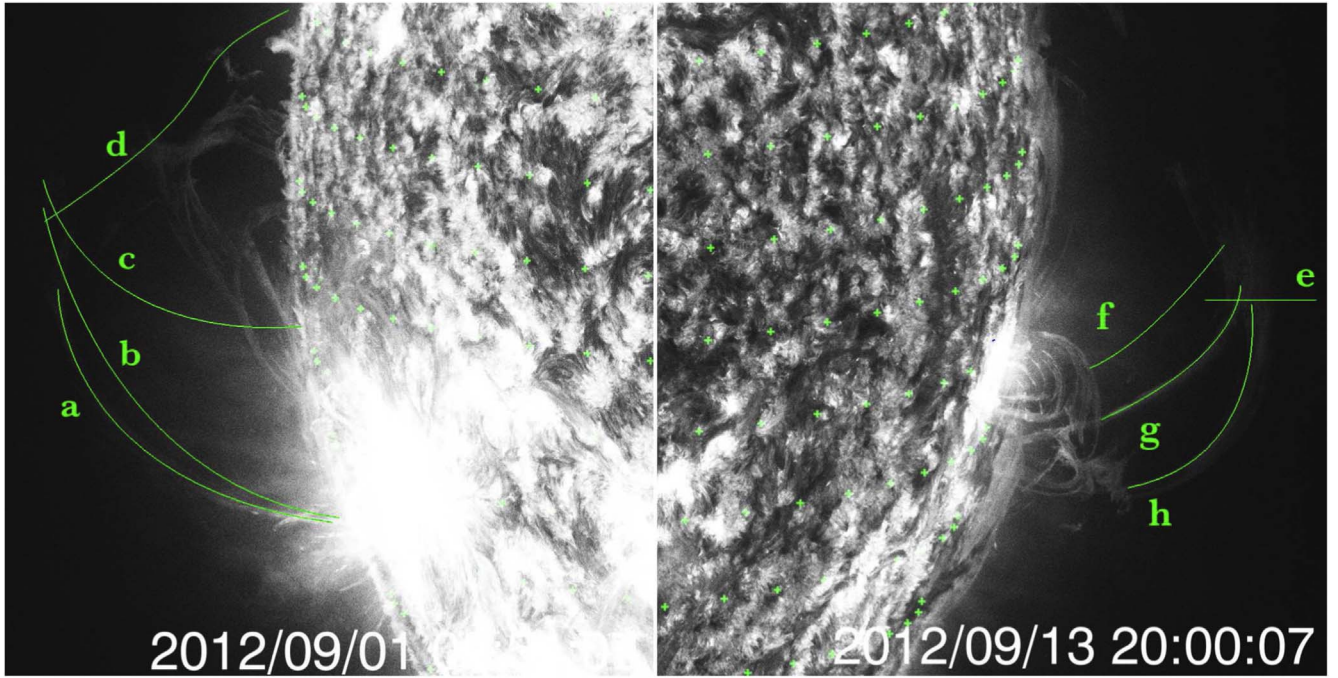


Figure 5. *SDO/AIA* image of coronal cloud prominences on the limb taken on 2012 September 1 (left panel) and 2012 September 13 (right panel), in the 304 Å channel. The panels show cuts used for the subsequent time-slice diagrams. Plus signs (+) mark a longitude–latitude grid with 5° separation on the Sun. The width of each cut is 7 pix \approx 3 Mm across. Each cut has its origin at the cloud and its length is measured downward along the curve.

The time-slice diagrams are generated by plotting as a function of time the brightness along the cut starting from the top toward the Sun. This is rectified in the panels and the distance or height in the ordinate corresponds to the length along the cut starting from the bottom. The panels show that the plasma motion occurs only downward with velocities from 20 km s^{-1} near the cloud's top up to 145 km s^{-1} near the solar surface. The lack of upward motions implies that the source of

the coronal cloud prominence plasma is not below the cloud itself (as is the case for other noncloud prominences). The observed plasma motions have velocities near the solar surface up to 145 km s^{-1} and accelerations that vary from 12 to 35 m s^{-2} . Similar velocities and accelerations for downflows of 304/ÅA coronal condensations along large-scale coronal loops were shown in Stenborg et al. (2008). The upper left image in Figure 7 shows the gradual formation of the coronal cloud

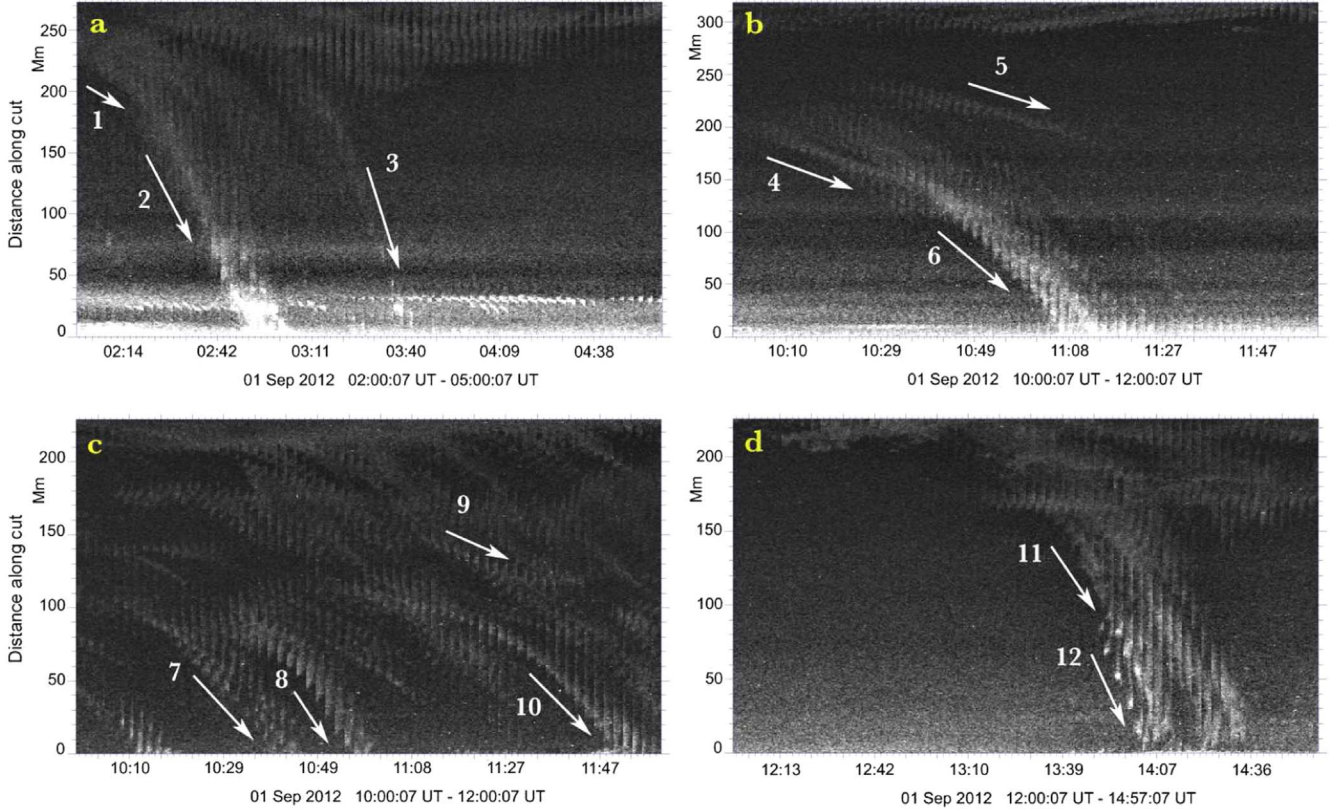


Figure 6. Time-slice diagrams for cuts #a-d from Figure 5 taken by SDO/AIA in the 304 Å channel with 1 minute cadence on 2012 September 1. White arrows outline downstreaming motions along the slices with numbered velocities: $V_1 = 30 \pm 3 \text{ km s}^{-1}$; $V_2 = 125 \pm 5 \text{ km s}^{-1}$; $V_3 = 145 \pm 5 \text{ km s}^{-1}$; $V_4 = 32 \pm 3 \text{ km s}^{-1}$; $V_5 = 23 \pm 3 \text{ km s}^{-1}$; $V_6 = 73 \pm 4 \text{ km s}^{-1}$; $V_7 = 56 \pm 3 \text{ km s}^{-1}$; $V_8 = 78 \pm 4 \text{ km s}^{-1}$; $V_9 = 28 \pm 3 \text{ km s}^{-1}$; $V_{10} = 60 \pm 3 \text{ km s}^{-1}$; $V_{11} = 74 \pm 4 \text{ km s}^{-1}$; $V_{12} = 88 \pm 4 \text{ km s}^{-1}$.

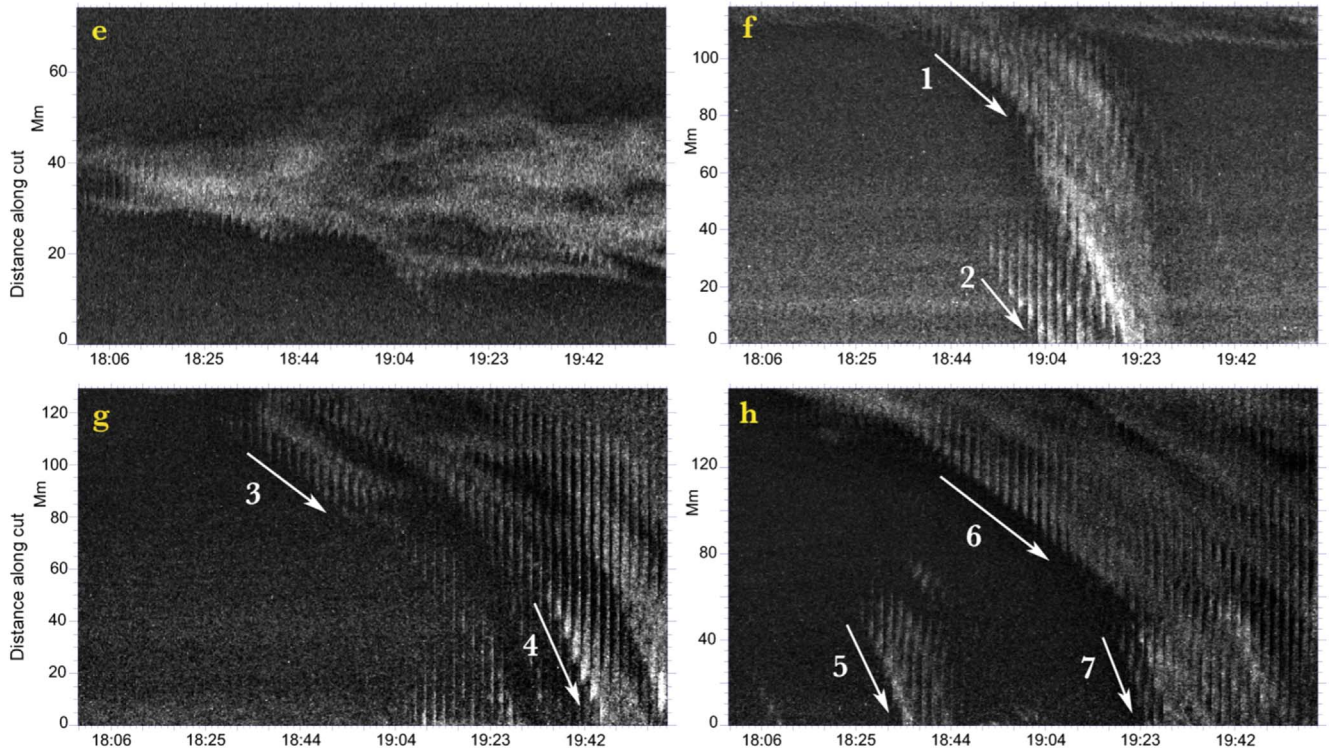


Figure 7. Time-slice diagrams for cuts #e-h from Figure 5 taken by SDO/AIA in the 304 Å channel with 1 minute cadence on 2012 September 13; 18:00:07 UT–20:00:07 UT. White arrows outline downstreaming motions along the slices with numbered velocities: $V_1 = 22 \pm 3 \text{ km s}^{-1}$; $V_2 = 36 \pm 3 \text{ km s}^{-1}$; $V_3 = 24 \pm 3 \text{ km s}^{-1}$; $V_4 = 66 \pm 4 \text{ km s}^{-1}$; $V_5 = 93 \pm 4 \text{ km s}^{-1}$; $V_6 = 30 \pm 3 \text{ km s}^{-1}$; $V_7 = 116 \pm 5 \text{ km s}^{-1}$.

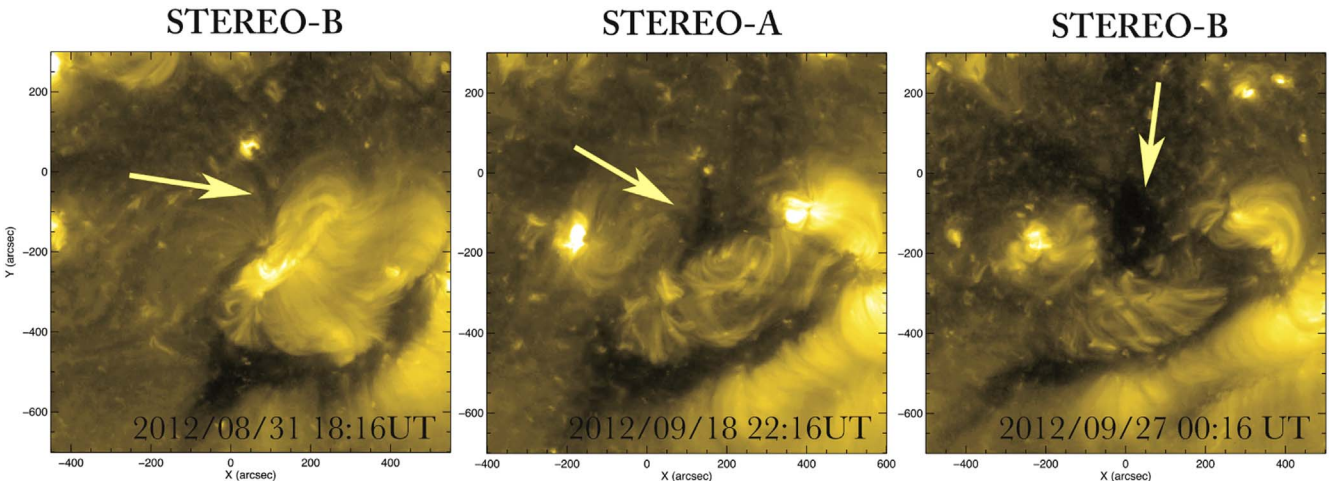


Figure 8. Funnel open field evolution into a regular coronal hole as observed by *STEREO/SECCHI* in the 284 Å band.

prominence along the radial cut #e on 2012 September 13. One can see that the process of formation occurs at heights of ~ 175 Mm ($\simeq 0.25 R_{\odot}$), and the cloud increases its width from 15 Mm to 35 Mm over a period of 2 hr. The downward flow starts about 40–60 minutes after the first appearance of the coronal cloud plasma (Figures 6, 7).

The calculated values of the velocities depend on the given slope in the time-slice diagram indicated by white arrows. These velocities correspond to only one value of ratio between changes in distance and in time, instantaneous velocities at the time resolution of the images $V = dl/dt$.

Cloud motions differ from motions associated with other observed coronal inflows, such as coronal rain. Wang et al. (1999) estimate plasma in coronal rain after CMEs to have inflow speeds of 20–100 km s $^{-1}$ or more; coronal rain is usually observed and measured at the heights of AR loops or solar filaments, ~ 45 Mm, as shown in Liu et al. (2012), and with average drainage velocity ~ 30 km s $^{-1}$. Finally, coronal rain does not appear to accelerate from a static floating plasma, rather it is falling as it appears, and may be connected to plasma flow along filament threads, for instance. In our paper the cloud formation original height lies in the interval ~ 140 –280 Mm, with average height ~ 210 Mm, which is far above the heights of active region or intermediate filament formation. The initial velocity of plasma in coronal clouds (at a height of 210 Mm) is \simeq zero, as shown by cut #e in Figure 7.

The just-described observations of coronal clouds forming in the same region for about four weeks pose the question as to what magnetic coronal configuration is required to support these metastable structures. Figure 8 shows images of the coronal cloud forming region on the disk as seen by *STEREO B*, *A*, and *B* again, in the 284 Å band at the end of August, mid-September, and the end of September. By the end of September—beginning of October, when coronal cloud prominences stopped forming, the region had become a well-developed round shaped coronal hole. On the other hand, in the first two images in Figure 8, the region can be seen as a very thin and elongated dark area, a narrow dark channel of open fields that must have been strongly expanding higher up in the corona, i.e., something resembling an elongated coronal magnetic funnel. As we will see in the coming section, this peculiar magnetic field structure appears to be the necessary ingredient

for the formation of coronal cloud prominences. The other ingredient is the eruptions providing the cloud mass.

3. Analysis of the Magnetic Structure of Funnels

To discuss the coronal magnetic field configuration in the area surrounding coronal cloud formation we will use a PFSS model (Schrijver & De Rosa 2003), that evolves the lower boundary magnetic field with a surface-flux transport model complementing observations. The source surface where the magnetic field becomes radial is situated at $r = 2.5 R_{\odot}$.

We have carried out PFSS reconstructions of the solar magnetic field for all of the dates corresponding to the coronal cloud observations discussed in the previous sections. As mentioned before, the coronal cloud forming region remained the same throughout the observation intervals presented in Table 1. Figure 9 shows a sequence of PFSS slices taken across the area above which the coronal cloud prominences formed, for the date of 2012 September 6 when the coronal cloud was observed by *STEREO-B*. The separation angle between *STEREO-B* and *SDO* was 116°, this allows us to observe the cloud formation region at the limb by *STEREO-B* and on the disk by *SDO* simultaneously. Each image in Figure 9 corresponds to a separate slice in the east–west direction at a fixed latitude across the coronal cloud forming region, with an extension of 5° in longitude and a width of 1°. The six images are separated by 3° in latitude and each image has been rotated to give a limb view of the corresponding latitude. One immediately sees that the coronal cloud forms in a region overlying the rapid expansion of a funnel shaped coronal hole neighboring closed magnetic field regions. The latitudinal extension of the hole is much greater than its width, as was already seen in the on-disk images of Figure 8. In addition, the height at which the coronal cloud formed, 0.2 – $0.3 R_{\odot}$, lies just above where the magnetic funnel opens up, “leaning” onto the neighboring closed field regions. We superimposed the coronal cloud prominence observed by *STEREO-B* in 304 Å on September 6 and the PFSS model calculated for the same time, rotated to get an east limb view (Figure 10). The coronal cloud prominence perfectly fits to the bottom of the funnel-like open field region. The plasma of the cloud is shown to accumulate at heights where the magnetic field lines diverge most rapidly, while the falling plasma trajectories seem to

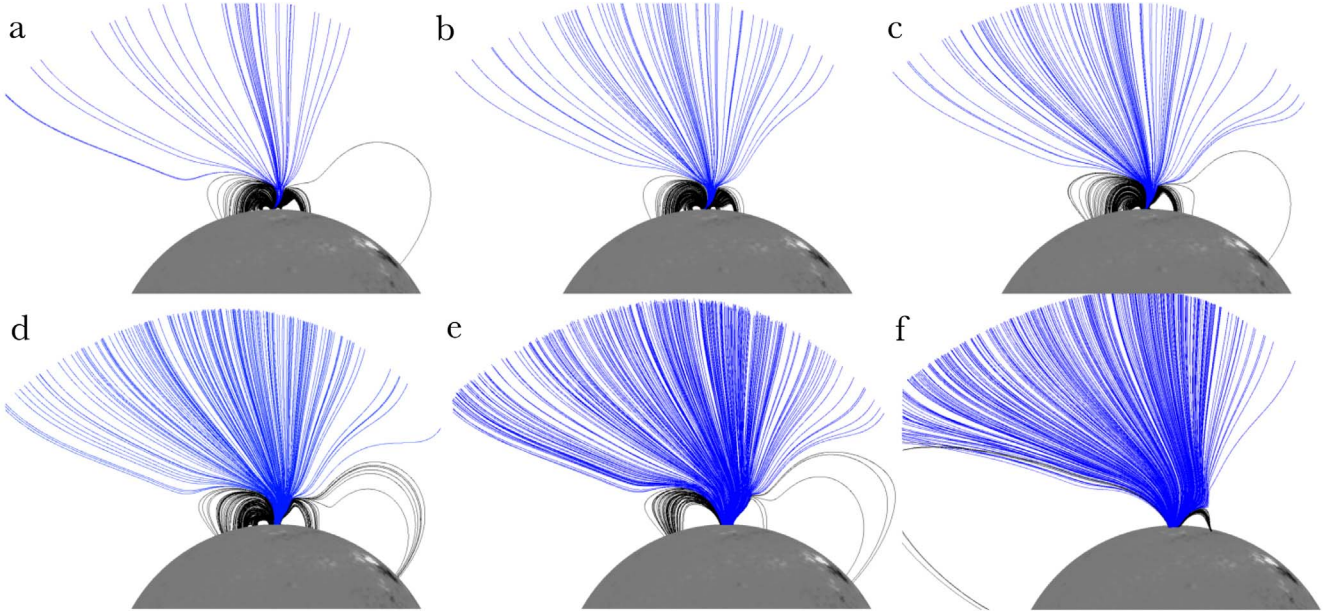


Figure 9. Funnel magnetic configurations of open field lines: a sequence of PFSS slices taken across the area above which the coronal cloud prominences formed, for the date of 2012 September 6. Each image has been rotated to give a limb view of the corresponding latitude.

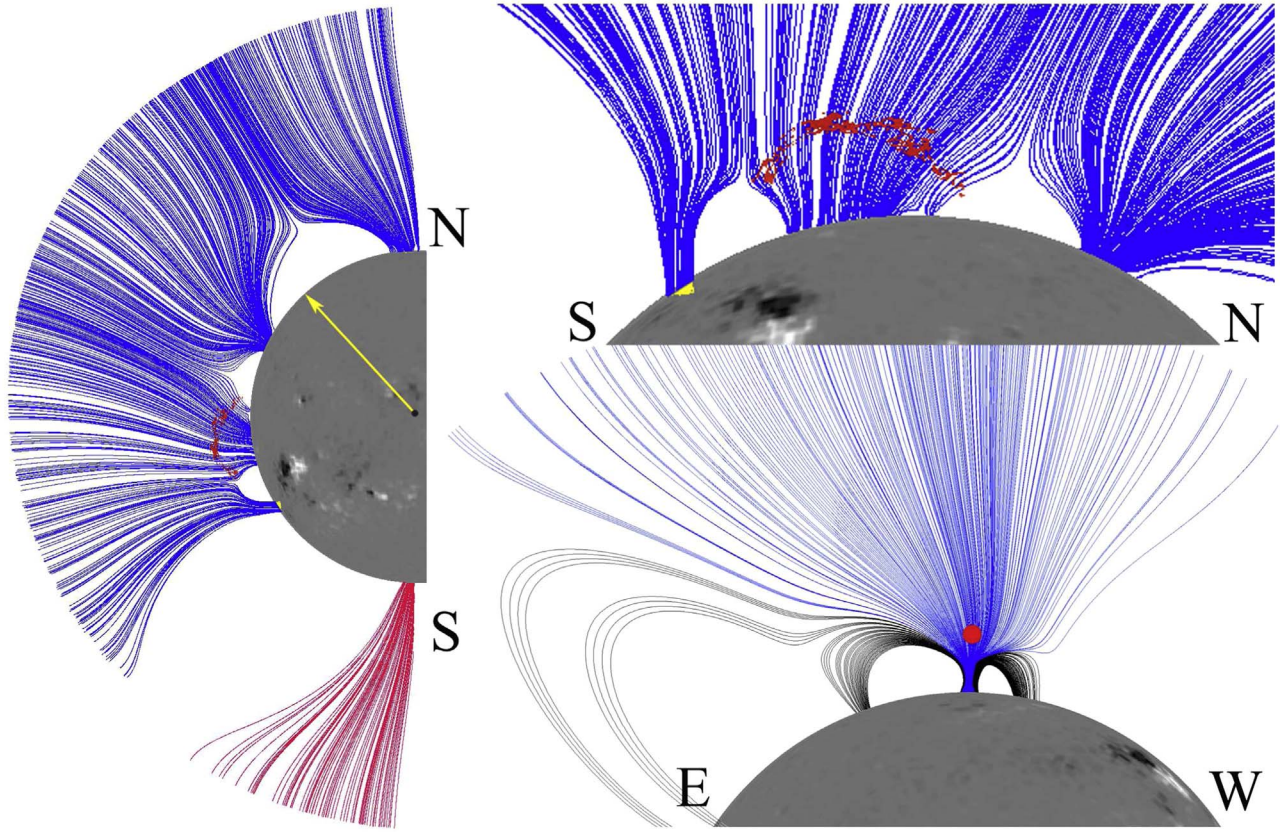


Figure 10. Superposition of the coronal cloud seen in 304 Å on 2012 September 6 (STEREO/SECHHI-B) and funnel magnetic field lines calculated using the PFSS model (from *SDO/HMI* magnetogram) on the same date and projected on the limb.

follow the bending closed field lines of the nearby filament channel arcades.

The funnel-like open magnetic field visible as a narrow coronal hole in the 284 Å band on August 31, evolved into a regular circular coronal hole one rotation later (Figure 8).

The magnetic field lines obtained via a PFSS extrapolation of the photospheric field on 2012 October 6 then display a more standard monotonic radial expansion—i.e., the magnetic funnel has disappeared (Figure 11). The fact that no coronal clouds seem to form in this location by the end of

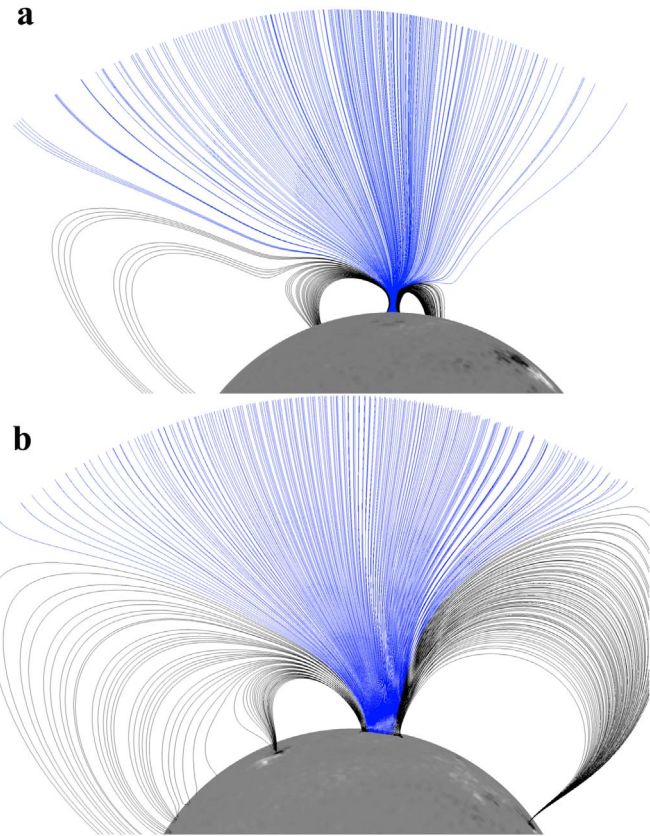


Figure 11. Comparison between funnel-like nonmonotonic (a) and regular open magnetic fields (b). The funnel open field (PFSS for September 6) evolved into a regular coronal hole one rotation later (PFSS for 2012 October 6). The magnetic field lines for a regular coronal hole (b) show monotonic radial expansion—no rapid funnel-like nonmonotonic expansion (PFSS field lines rotated to give a limb view).

September—beginning of October strongly supports the conclusion that this results from the changes in magnetic field geometry and expansion of the open field lines.

The coronal cloud develops in what is therefore a peculiar open magnetic field region, onto a background of stratified coronal plasma, which expands into the solar wind. In the force balance, which will be discussed in detail in the following section, a very important role is played by the rate of expansion of neighboring magnetic field flux bundles within the funnel. This expansion factor, defined as $\varepsilon_f = (R_\odot^2/R^2)(B_\odot/|B_r|)$, is plotted in Figure 12 as a function of radial distance along an ensemble of field lines of the coronal funnel for the same date as Figures 9 and 10. The red curves are for the September period when the funnel was present, the black curves show field lines from the same region one rotation later, when the funnel had disappeared. One sees that for most of the field lines (curves in red), excepting the ones at the center of the funnel, the profile is strongly nonmonotonic with a peak in the expansion at $\sim 0.2 R_\odot$, where a local maximum occurs, i.e., where the funnel magnetic configuration fans out (Figure 12, top left panel). Also shown in Figure 12 are the profiles of the magnetic pressure along different funnel and nonfunnel field lines (red and black, respectively, top right), and corresponding solar wind speed profiles (bottom left) and kinetic pressure profiles. One is struck immediately by the presence of a local magnetic pressure minimum, only seen for the field lines with corresponding peak in the expansion factor. This plays a major

role in the force balance for the cloud plasma, as will be discussed in the next section. Our solar wind models do not take into account the presence of the cloud; however, they also show the breaking of the wind where expansion is maximized. The details of the solar wind emanating from funnels will be explored elsewhere, though we mention here that the funnel only gives rise to slow solar wind, because of the breaking in the profile and subsequent reacceleration much further out (see, e.g., Wang 1994; Panasenco & Velli 2013; Wang & Panasenco 2019).

4. Forces on Clouds in Magnetic Funnels

We have seen that clouds form in the presence of funnel magnetic fields, so this provides a hint to understand the forces that may be in play. Naturally, the dynamics of the coronal cloud prominence plasma depends also on the magnetic field structure of the cloud plasma itself. The cloud prominence material may thread the open, funnel-like magnetic field either completely, partially, or not at all. In the first case, the main forces acting on the cloud plasma, besides gravity, would be those due to the gas pressure of the ambient plasma (leading to an Archimedes effect), with possible contributions to the pressure coming from a flux of waves (for example, the Alfvén waves thought to be responsible for solar wind acceleration), drag-type forces, and the large-scale $\mathbf{J} \times \mathbf{B}$ force. The most likely situation, however, is either the second or third case where one may speak of either magnetically isolated or partially isolated plasmoids, given the observation that cloud plasma appears as a result of neighboring eruptions. In this case the cloud motion is accompanied by a deformation of the field outside the cloud that induces currents. The currents are localized at the cloud–outer field interface and therefore take the form of a current sheath, localized where the stresses are maximum. The effect of such currents is to produce a force, known as the diamagnetic (or melon-seed) effect (Parker 1954, 1957; Pneuman 1983; Cargill & Pneuman 1984; Pneuman & Cargill 1985). Such currents may end up heating the cloud as well.

To estimate the forces on the cloud, consider the equation of motion for the plasma in the corona described as a magnetohydrodynamic flow:

$$\rho \left(\frac{\partial \mathbf{u}}{\partial t} + \mathbf{u} \cdot \nabla \mathbf{u} \right) = -\nabla p + \frac{1}{c} \mathbf{J} \times \mathbf{B} + \rho \mathbf{g}. \quad (1)$$

Here ρ is the density, \mathbf{u} is the local plasma velocity, p is the pressure, \mathbf{J} , \mathbf{B} are the current density and magnetic field, respectively, while $\mathbf{g} = -(GM_\odot/R^2)\mathbf{e}_r$ is the local gravitational acceleration directed radially toward the Sun. Along the open field lines of the magnetic funnel one can imagine that this plasma, in the absence of the clouds, may be described by a stationary outflow giving rise to solar wind at large distances (acceleration profiles are shown in the bottom left of Figure 12).

Typical parameters for solar wind models along such open field lines (Hansteen & Velli 2012) give number densities at the height of $1.2 R_\odot$ between $1.5 \cdot 10^6 - 10^7$ with a temperature (ion and electron averaged) around $2 \cdot 10^6$ K. Wind speeds are typically $u \lesssim 100 \text{ km s}^{-1}$, to be compared with the thermal speed, $u_s \sim 220 \text{ km s}^{-1}$, and the Alfvén speed, $V_a \lesssim 2000 \text{ km s}^{-1}$. Therefore, the cloud dynamics we are discussing within a fraction of a solar radius from the surface occurs well below the sonic point, and it is well known that in such cases the plasma outflow velocity may be

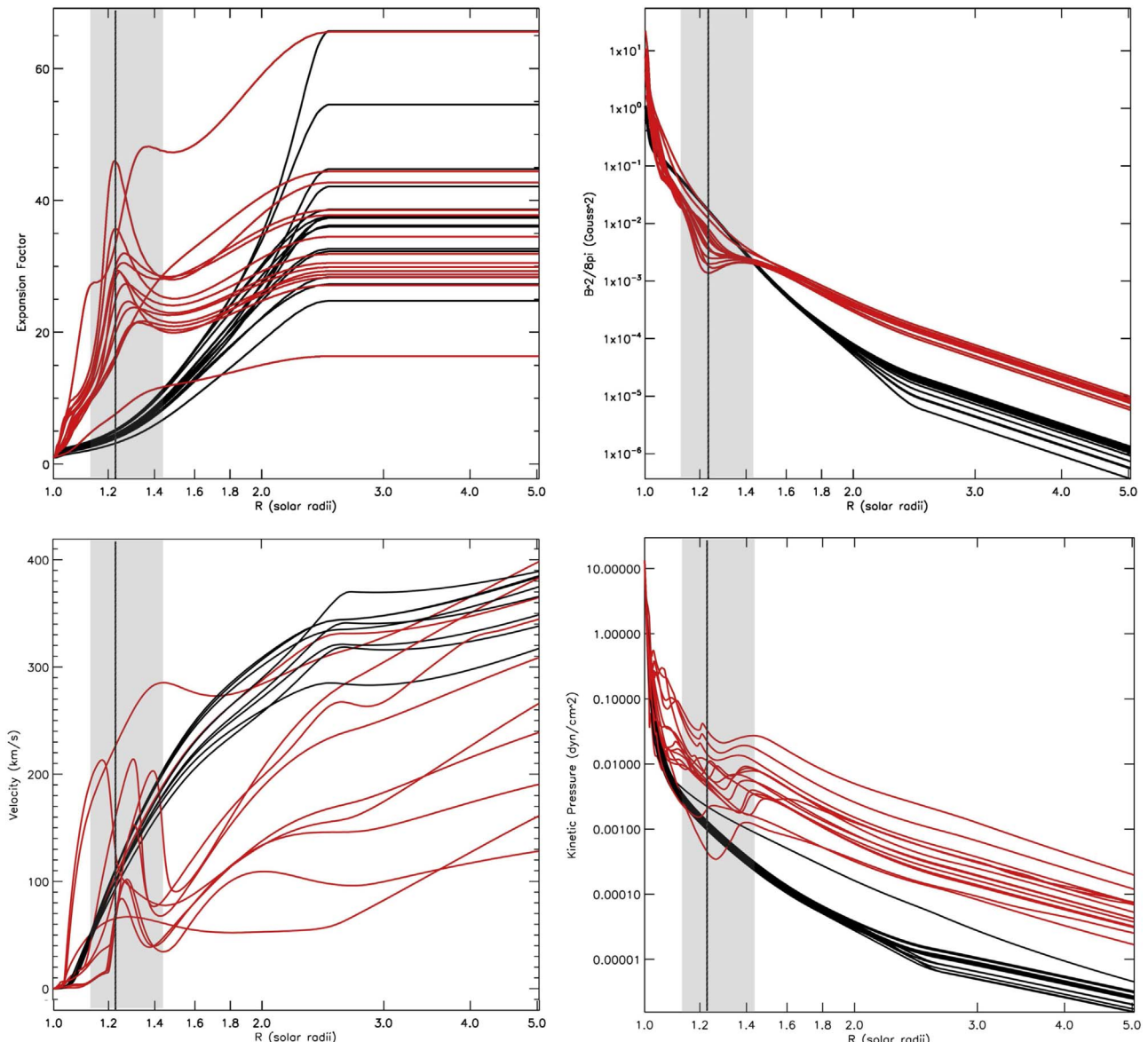


Figure 12. Contrast between configurations with and without a magnetic funnel is shown via a solar wind field-aligned model calculated using field lines from both the funnel structure before (red lines) and the regular coronal hole that developed later (black). Upper left panel: magnetic funnel field line expansion factors were calculated for 35 open field lines derived from the *SDO/HMI* magnetogram (2012 September 6, 18:04 UT). The local extremum is at $\sim 1.2 - 1.3 R_\odot$. This is the exact height where the coronal cloud prominences begin to form inside this funnel (X -axis: $r_s = R_\odot$). Upper right panel: the magnetic pressure is a rapidly increasing function toward the solar surface, and in fact for the bulk of the funnel field lines has a minimum corresponding to the maximum expansion rate of the funnel, in the neighborhood of $0.25 R_\odot$ above the solar surface. Beyond the source surfaces a spherical expansion is assumed. Bottom left panel: solar wind speed profile along the chosen field lines. Note how the rapid funnel expansion causes the solar wind to slow down in the neighborhood of expansion factor peaks. Bottom right panel: kinetic pressure profiles along the same set of field lines.

neglected as far as the stratification in this region is concerned. Therefore, the stratification may be considered static, albeit with a slight modification coming from the field-aligned $\mathbf{J} \times \mathbf{B}$ forces resulting from outwardly propagating waves.

For a coronal cloud the number densities must be at least one or even up to two orders of magnitude higher than the background corona, so that any archimedes effect will be small. We have seen that the forming coronal cloud prominence plasma first appears and then tends to drain by escaping the funnel field. The local gravitational acceleration at a height of $1.2 R_\odot$ is 162 m s^{-2} , which is much greater than any kind of acceleration (by factors of 5–10), which can be measured from the time-slice diagrams of Figures 6 and 7 (even taking into account the projection effects due to the nonradial nature of the

cuts). The only force that would appear strong enough is that due to the deformation of the open field caused by the diamagnetic nature of the plasmoids.

To calculate the force on an individual plasma element of the cloud, one must integrate the equation of motion over the volume of the cloud in question. Some assumption must be made on the shape of the cloud and its deformability, and then one may separate out the global force acting on the cloud center of mass from forces and moments causing deformation of the cloud itself. Such an analysis was first carried out by Parker (1954, 1957) and then in a series of papers by Pneuman (1983), Cargill & Pneuman (1984), and Pneuman & Cargill (1985) considering prolate spheroid shaped clouds. The result of the integral of the pressure terms (kinetic pressure, pressure

resulting from the ponderomotive force due to a wave flux along the open funnel field lines) is an effective archimedes force due to the density difference between the cloud and the background plasma, which acts to reduce the effect of gravity somewhat. If the cloud is magnetically connected to the funnel, then the cloud particles may slip freely along the open field lines without violating the flux conservation theorem, and the only remaining force term is a drag due to the effect of electromagnetic fluctuations induced by the cloud motion and collisions. If the cloud is at least partially magnetically isolated on the other hand, a surface current develops between the cloud elements and the ambient plasma resulting in the diamagnetic (DM) or melon-seed force (Schmidt & Cargill 2000; Rappazzo et al. 2005).

The diamagnetic force arises from the volume integral of the Lorentz force over the cloud

$$\int_V \frac{1}{c} \mathbf{J} \times \mathbf{B} dV = \int_V \left(\frac{\mathbf{B} \cdot \nabla \mathbf{B}}{4\pi} - \nabla \frac{\mathbf{B}^2}{8\pi} \right) dV. \quad (2)$$

Because the stresses develop mostly in the neighborhood of the cloud boundary, where currents become singular, this expression may be well approximated (see, e.g., Pneuman & Cargill 1985) with the bounding surface integral of the (integrated) stresses, and the force per unit volume on the cloud is obtained by dividing that integral by the cloud volume to obtain:

$$\mathbf{F}_{\text{DM}} = \frac{1}{V} \int_S \left[\mathbf{B}_e \frac{\mathbf{B}_e}{4\pi} \cdot d\mathbf{S} - \frac{\mathbf{B}_e^2}{8\pi} d\mathbf{S} \right]. \quad (3)$$

Here \mathbf{B}_e is the magnetic field at the boundary between the cloud and the external field. If the plasma cloud parcels are small, the external field deformation may be neglected and the unperturbed external field may be used to get a good estimate of this force (Pneuman & Cargill 1985). This may then be written as

$$\mathbf{F}_{\text{DM}} = -k \nabla \frac{\mathbf{B}_e^2}{8\pi}, \quad (4)$$

where we have introduced a factor $k \leq 3/2$ to include the effects of cloud shape (Pneuman & Cargill 1985) and partial isolation of the cloud. This force is directed along the gradient of the external, deformed field (e denotes the field external to the cloud) pushing the cloud in the directions of weaker field.

Now the fastest way to appreciate the relative intensity of the terms in the force balance is to compare each of them to the gravitational force. In particular we may write the gravitational force intensity as

$$F_G = \frac{1}{2R_\odot} \frac{V_{\text{esc}}^2}{R^2} \alpha \rho_{\text{cl}}, \quad (5)$$

where V_{esc} is the escape speed from the Sun, the height R is measured in units of the solar radius, and $\alpha \lesssim 1$ corrects for the effective Archimedes force. On the other hand, the intensity of the diamagnetic force may be written as

$$F_{\text{DM}} = \frac{k}{2R_\odot} \frac{V_a^2}{l_{B^2}} \rho, \quad l_{B^2} = \left| \frac{R_\odot}{B^2} \nabla B^2 \right|^{-1}, \quad (6)$$

where l_{B^2} is the scale height of the (unperturbed) magnetic field pressure (or energy, also in units of solar radius).

The ratio of the diamagnetic to gravitational forces therefore becomes

$$\frac{F_{\text{DM}}}{F_G} = k \left(\frac{V_a}{V_{\text{esc}}} \right)^2 \frac{R^2}{l_{B^2}} \frac{\rho}{\rho_{\text{cl}}}. \quad (7)$$

Consider then a typical Alfvén speed $V_a \simeq 7.5 \cdot 10^2 \text{ km s}^{-1}$ while the escape speed from the Sun is $\simeq 618 \text{ km s}^{-1}$, then we find

$$F_{\text{DM}}/F_G \simeq 2.5 k \rho / (\rho_c l_{B^2}). \quad (8)$$

Considering a density ratio of cloud to corona $\rho_c/\rho \simeq 10$, and a factor $k \simeq 0.5$ we find for the diamagnetic force to balance the gravitational force the magnetic energy scale height in the neighborhood of the maximum expansion rate of the magnetic funnels must be, in the worst case scenario,

$$l_{B^2} \lesssim \frac{1}{8}, \quad (9)$$

i.e., an eighth of a solar radius, which is amply satisfied (see Figure 12, top right panel) for our funnel geometry. If the Alfvén speed is twice as large, which could easily be the case for our funnel, then the critical magnetic scale height is reduced to only one-half a solar radius, showing how important this effect is.

Given that the effective magnetic energy scale height l_{B^2} just below the dip is closer to 0.05 solar radii, the cloud density could reach factors of up to 50 and still be stopped in its fall by the diamagnetic force. As written above, this force is simply the gradient of a potential, so one may use the magnetic field model described above to find regions where the magnetic cloud plasma could end up being trapped in equilibrium. The effective potential is the sum of $kB^2/8\pi$ and the gravitational potential $-GM_\odot \alpha \rho_{\text{cl}}/R$.

The magnetic component of the potential is a rapidly increasing function toward the solar surface, and in fact for the bulk of the funnel field lines has a minimum corresponding to the maximum expansion rate of the funnel, in the neighborhood of $0.2 R_\odot$ above the solar surface (Figure 12, top right). The plasma falling from above can reach this local minimum but cannot penetrate much lower inside the funnel because of the rapid increase of the diamagnetic force in the central regions of the funnel. Thus, the magnetic levitation of (partially) diamagnetic clouds provides the simplest way of understanding of the formation of coronal cloud prominences in coronal funnel fields.

However, it is very difficult for the magnetic forces and the gravitational force to balance exactly: the gravitational force is along the radial direction, while the diamagnetic force pushes in the direction of weaker field, and will generally form an angle to the radial, typically away from the funnel center in the fanning out direction. The result is a metastable situation, with plasma continuously being pushed sideways through weaker field regions as it falls, and then along the nearby closed fields back to the Sun and observed as large-scale coronal cloud rain falling down from the height of $0.2 R_\odot$ above the solar surface. This effect may be compounded by the dissipation of the currents at the cloud surfaces and the reconnection of field lines in the funnel outskirts, providing the spider-like appearance of the falling cloud material.

The downflows described in this paper are related to CMEs and filament eruptions but the connection is not as straight-forward as

in the studies of Liu et al. (2015), where coronal rain is immediately seen to result from plasma falling back after a filament eruption: in that case no cloud prominences become visible, because of the absence of funnel fields, and no levitation is provided in the corona. The falling plasma may only be slowed down by drag with the ambient corona.

5. Conclusions

We have found and described peculiar open coronal magnetic field geometries displaying an open funnel configuration where the magnetic field expansion is nonmonotonic and dips in the magnetic pressure profile with height are formed. We have shown that such funnels are sites of coronal cloud prominence formation. The main ingredients required for the development of such a peculiar topology is the presence of one or multiple pseudostreamers. On the other hand, the nature of CMEs from pseudostreamers and corresponding inflows lead tiny parcels of inflowing plasma to accumulate in neighboring magnetic funnels. The sources of the coronal cloud prominence plasma are prior eruptions, surges, flares capable of propelling the prominence plasma high enough into the corona, where, however, plasma without sufficient velocity then falls back, carrying whatever magnetic field is associated with it. Diamagnetic currents then slow it down and allow it to levitate on the open lines of the magnetic funnel. The observed plasma motions are always directed downward and have velocities near the solar surface up to 145 km s^{-1} and accelerations (along the cuts we have shown) which vary from 12 to 35 m s^{-2} .

The formation time (\sim an hour) and lifetime (\sim many hours) of individual coronal cloud prominence blobs are too short to explain the survival of coronal cloud prominences at the same location over 18 consecutive days during the limb to limb passage observed by *STEREO* and *SDO* without a source replenishing them. The most plausible explanation that fits the observations is that the plasma inside the magnetic funnel is constantly replenished through nearby eruptions and inflows in their wakes. These eruptions do not have to be major ones; however, fast eruptions usually produce a substantial amount of plasma that eventually falls back to the Sun, due to too fast expansion of the magnetic structure that leads to a significant component of the velocities in the nonradial direction. The visibility of the inflows depends on the amount, density, and trajectories of material that falls back after eruptions. The very faint low-density features in pseudostreamer events suggest that more inflows may be present at or below the noise level of current instruments (Wang & Hess 2018a, 2018b). The inflows in the wake of pseudostreamer CMEs are weaker and more dispersed compare to streamer CMEs because of the specific magnetic topology of pseudostreamers and ray-like structure of pseudostreamer CMEs (Wang 2015). The lower height of pseudostreamer CME sources (i.e., the generally lower height of the confining arcades) implies that stronger CME deflection may occur in the low corona below $3\text{--}4 R_\odot$, and the low-density inflows will disperse more widely compared to helmet CME inflows. High resolution spectroscopic observations in the lower corona with DKIST (Daniel K. Inouye Solar Telescope) should provide such missing observations.

The 2012 August 31 eruption is a case in point. In this case the sky projected CME speed was a hefty $\sim 1100 \text{ km s}^{-1}$ but the nonradial deflection toward the magnetic funnel was also strong, $\sim 40^\circ$. Simple estimates of the various forces in play show that the most reasonable assumption for the coronal cloud

prominence levitation is the diamagnetic force, which can be far greater than the pressure gradients or archimedes force on the much denser coronal cloud at $R = 1.2 R_\odot$. The diamagnetic force dominates the balance and can easily provide a metastable or quasi-equilibrium state for small cloud elements accumulating gradually in the neighborhood of the maximum expansion of the open field lines. In addition, the directional mismatch between the diamagnetic force and gravity naturally explains the draining of the coronal cloud away from the funnel center and above the closed field lines on which the funnel field “leans.”

The sequence of coronal cloud prominences was observed in the same location by *SDO* and *STEREO* in the period 2012 August–September, but disappeared before the *STEREO-A* observations of the west limb in October. What could have caused this change? The main structural change of the background corona during this period was the disappearance of the funnel-like structure. The open field lines became more regular, corresponding to a coronal hole with a monotonic open field line expansion and a smaller gradient of the field. This made it much more difficult for ejected plasma to penetrate the coronal hole field lines and removed the presence of metastable equilibria where the falling plasma could accumulate to become observable as a coronal cloud.

O.P. and A.P. were supported in this research under the NASA SPP program. O.P. was also supported by the NSF EAGER grant No. 1853530. M.V. was supported by the NASA Parker Solar Probe Observatory Scientist grant No. NNX15AF34G. We thank the referee for very helpful comments. The SECCHI data are produced by an international consortium of the NRL, LMSL and NASA GSFC (USA), RAL and Univ. Bham (UK), MPS (Germany), CSL (Belgium), IOTA and IAS (France). The AIA data used here are courtesy of *SDO* (NASA) and the AIA consortium.

ORCID iDs

Marco Velli <https://orcid.org/0000-0002-2381-3106>

References

- Allen, U. A., Bagenal, F., & Hundhausen, A. J. 1998, in ASP Conf. Ser. 150, IAU Coll. 167, New Perspectives on Solar Prominences, ed. D. F. Webb, B. Schmieder, & D. M. Rust (San Francisco, CA: ASP), 290
- Cargill, P. J., & Pneuman, G. W. 1984, *ApJ*, 276, 369
- Engvold, O. 1976, *SoPh*, 49, 283
- Hansteen, V. H., & Velli, M. 2012, *SSRv*, 172, 89
- Hess, P., & Wang, Y.-M. 2017, *ApJ*, 850, 6
- Liewer, P., Panasenco, O., Vourlidas, A., & Colaninno, R. 2015, *SoPh*, 290, 3343
- Liewer, P. C., Panasenco, O., & Hall, J. R. 2013, *SoPh*, 282, 201
- Lin, Y., Martin, S. F., & Engvold, O. 2006, *BAAS*, 38, 219
- Liu, W., Berger, T. E., & Low, B. C. 2012, *ApJL*, 745, L21
- Liu, W., De Pontieu, B., Vial, J.-C., et al. 2015, *ApJ*, 803, 85
- Mackay, D. H. 2005, in ASP Conf. Ser. 346, Large-scale Structures and their Role in Solar Activity, ed. K. K. Sankarasubramanian, M. Penn, & A. Pevtsov (San Francisco, CA: ASP), 177
- Panasenco, O., Martin, S., Joshi, A. D., & Srivastava, N. 2011, *JASTP*, 73, 1129
- Panasenco, O., Martin, S. F., Velli, M., & Vourlidas, A. 2013, *SoPh*, 287, 391
- Panasenco, O., & Velli, M. 2010, in AGU Fall Meeting (Washington, DC: AGU), SH51A-1663
- Panasenco, O., & Velli, M. 2013, in AIP Conf. Proc. 1539, Solar Wind 13, ed. G. P. Zank et al. (Melville, NY: AIP), 50
- Parker, E. N. 1954, *PhRv*, 96, 1686
- Parker, E. N. 1957, *ApJS*, 3, 51
- Pneuman, G. W. 1983, *ApJ*, 265, 468
- Pneuman, G. W., & Cargill, P. J. 1985, *ApJ*, 288, 653

- Rappazzo, A. F., Velli, M., Einaudi, G., & Dahlburg, R. B. 2005, *ApJ*, **633**, 474
Saito, K., & Tandberg-Hanssen, E. 1973, *SoPh*, **31**, 105
Schmidt, J. M., & Cargill, P. J. 2000, *JGR*, **105**, 10455
Schrijver, C. J., & De Rosa, M. L. 2003, *SoPh*, **212**, 165
Sheeley, N. R., Jr., & Wang, Y.-M. 2002, *ApJ*, **579**, 874
Sheeley, N. R., Jr., & Wang, Y.-M. 2014, *ApJ*, **797**, 10
Stenborg, G., Vourlidas, A., & Howard, R. A. 2008, *ApJ*, **674**, 1201
Török, T., Panasenco, O., Titov, V. S., et al. 2011, *ApJL*, **739**, L63
Wang, Y.-M. 1994, *ApJL*, **437**, L67
Wang, Y.-M. 2015, *ApJL*, **803**, L12
Wang, Y.-M., & Hess, P. 2018a, *ApJ*, **853**, 103
Wang, Y.-M., & Hess, P. 2018b, *ApJ*, **859**, 135
Wang, Y.-M., & Panasenco, O. 2019, *ApJ*, **872**, 139
Wang, Y.-M., Sheeley, N. R., Jr., Howard, R. A., Cyr, O. C., St., & Simnett, G. M. 1999, *GeoRL*, **26**, 1203
Wang, Y.-M., Sheeley, N. R., Jr., & Rich, N. B. 2007, *ApJ*, **658**, 1340